


Article

Derivation and Validation of Bandgap Equation Using Serpentine Resonator

Junmin Yu ¹, Jaesoon Jung ² and Semyung Wang ^{1,*}

¹ School of Mechanical Engineering, Gwangju Institute of Science and Technology, 123 Cheomdangwagi-Ro, Buk-Gu, Gwangju 61005, Korea; pragen0525@gist.ac.kr

² Agency for Defense Development, Daejeon 34186, Korea; jjung91@add.re.kr

* Correspondence: smwang@gist.ac.kr; Tel.: +82-60-712-2390; Fax: +82-62-715-2384

Abstract: Bandgap refers to a frequency band where free waves do not propagate. One of the characteristics of a bandgap is its ability to block the propagation of bending waves in a specific frequency band with a periodic structure. Additionally, it has been reported in previous studies that the vibration-reduction performance of a bandgap is superior to that of other reduction methods. A bandgap can be generated in various frequency bands through a simple parameter change in the unit structure. However, the bandgap for a desired frequency band can be determined accurately only with intensive simulations. To overcome this limitation, we have mathematically derived the bandgap using a serpentine spring as a unit structure. The bandgap equation is derived from the general mass–spring system and the final bandgap is derived by substituting the system into the serpentine resonator. The error map for the major design parameter is confirmed by comparing the derived bandgap with the simulation result. In addition, the theoretical bandgap is compared to the experiment value and the vibration-reduction performance of the serpentine resonator is also confirmed. Based on the theoretical and experimental result, the proposed serpentine resonator verifies that the bandgap can be derived mathematically without numerical analysis. Therefore, serpentine resonator is expected to have various applications since it dramatically reduces the time and cost for forming the bandgap of the desired frequency band.

Keywords: bandgap; serpentine resonator; vibration; frequency band



Citation: Yu, J.; Jung, J.; Wang, S. Derivation and Validation of Bandgap Equation Using Serpentine Resonator. *Appl. Sci.* **2022**, *12*, 3934. <https://doi.org/10.3390/app12083934>

Academic Editor: César M. A. Vasques

Received: 15 February 2022

Accepted: 12 April 2022

Published: 13 April 2022

Publisher's Note: MDPI stays neutral with regard to jurisdictional claims in published maps and institutional affiliations.



Copyright: © 2022 by the authors. Licensee MDPI, Basel, Switzerland. This article is an open access article distributed under the terms and conditions of the Creative Commons Attribution (CC BY) license (<https://creativecommons.org/licenses/by/4.0/>).

1. Introduction

A metamaterial is defined as an artificial material with wave manipulation that does not exist in nature. Numerous studies have been conducted in various fields, such as electromagnetic [1–3], optical [4–6], and acoustic [7–10] to understand the characteristics of metamaterials. Among them, acoustic metamaterials have attracted significant attention in the vibro-acoustic field [11–15] due to their unique characteristics based on mechanism. The bandgap, one of the important characteristics of acoustic metamaterials, blocks the propagation of free bending waves of the host structure in a specific frequency region. Therefore, bandgap materials have a significant attenuation performance and are widely used in noise-, vibration-, and harshness-treatment procedures [16–21].

A bandgap can be generated by periodically arranging structures, such as resonators and scatterers, and inertial amplification. These structures make the wavenumber in the bandgap region imaginary, and consequently the bending wave becomes an evanescent wave and becomes dissipated, and the response of the host structure decreases in the bandgap region [22–25]. Therefore, an equation for the bandgap can be derived even though the wavenumber of the bending wave in the host structure becomes imaginary. The equation is derived from the resonance frequency of the periodic structure and mass ratio between the host and periodic structures [26]. Since it is difficult to control the mass ratio, the resonance frequency of the resonator plays an important role in the formulation

of the equation. Thus, the parameters of the periodic structures are important design parameters for determining the bandgap, and the bandgap can be controlled by adjusting the parameters.

In spite of the wave manipulation properties of metamaterials, there is no adequate method to formulate the bandgap yet. Most metamaterials set the attenuation frequency region and determine the unit structure design in which the bandgap is implemented using high levels of simulation. Although this method is the most accurate, the simulations are time-consuming. To overcome this limitation, we have derived the equation of the bandgap mathematically to implement the bandgap in the desired frequency region by controlling the structural parameters. This equation helps to modularize the parameters of the bandgap region and reduce the time required for structural design.

In this study, the experimental analysis is implemented using a serpentine spring composed of meandering beams as a resonator to generate the bandgap. Serpentine springs are primarily used in various research fields due to their high stretchability and increased utility in narrow spaces [27–30]. In addition, the presence of various parameters in the serpentine spring provides adequate freedom to design the bandgap. Hence, we have derived the bandgap equation of the serpentine resonator and analytically verified it using a commercial software COMSOL. The relative errors between the numerical and analytical results are also analyzed. Additionally, the trend of the relative error when the design variables are modified is also identified to determine the most optimal design conditions. Finally, the results obtained are validated experimentally for similar design conditions and the theoretical equation is verified through the experiment. The experimental results show that the bandgap can be derived by an equation and the bandgap of the serpentine resonator can be successfully implemented.

This paper is organized as follows. Section 2 presents the mathematical derivation of the equation of the bandgap for a serpentine resonator. Section 3 formulates the numerical derivation of the bandgap and analyzes the relative error. Section 4 describes the experimental setup for the validation and demonstrates the performance of the serpentine resonator. Finally, Section 5 presents the conclusions with a discussion and suggestions for future work.

2. Theory

2.1. Bandgap

Figure 1 shows the plate on which the mass–spring resonators are uniformly distributed. Assuming that the resonators are infinitely periodic and smaller than the wavelength of interest, the equations of motion can be divided into two parts as:

$$\rho h \ddot{w}_p + D \nabla^4 w_p = f_{pr}, \quad (1a)$$

$$k_r(w_p - w_r) = m_r \ddot{w}_r = f_{rp}, \quad (1b)$$

where ρ is mass density, h is the thickness of the plate, w_p and w_r are the vertical displacements of the plate and resonator at the connection point, respectively, D is the bending stiffness of the plate, f_{rp} and f_{pr} are the forces of the resonator on plate and plate on resonator, and m_r and k_r are the lumped mass and stiffness of resonator, respectively.

The vertical displacement of the plate for the harmonic wave is defined as

$$w_p(x, y, t) = \bar{w}_p(x, y) \exp(j\omega t) \quad (2)$$

where ω is the angular frequency. By substituting acceleration with displacement in Equation (2), Equation (1a) can be modified as:

$$\left(\nabla^4 - \omega^2 \rho h / D \right) \bar{w}_p(x, y) = \frac{f_{pr}}{D}, \quad (3)$$

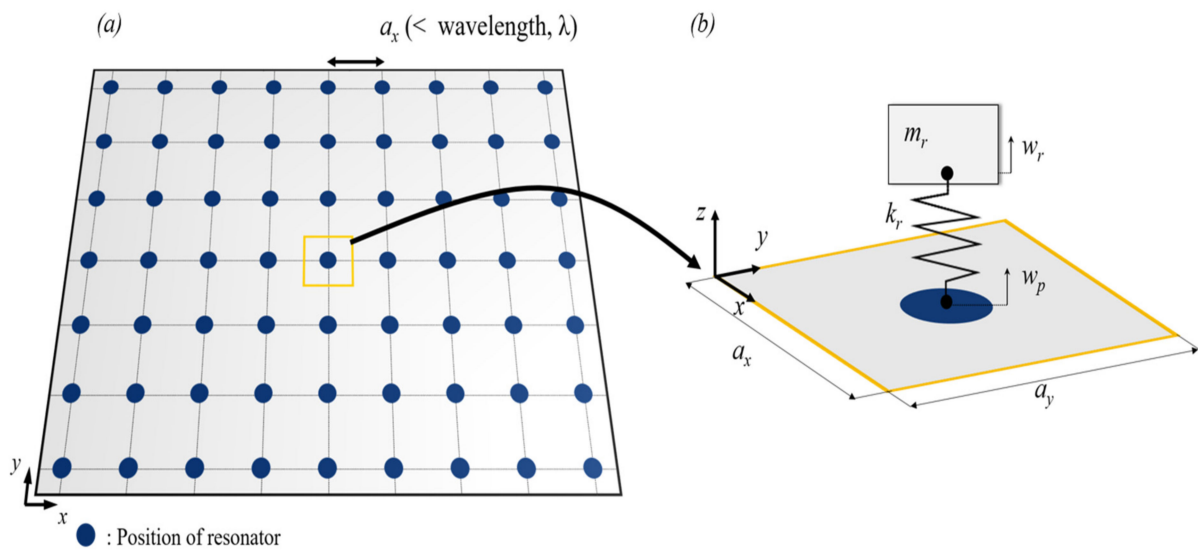


Figure 1. (a) Bandgap structure and (b) mass–spring resonator represented by the blue circle.

The wavenumber of the free bending wave in the plate k_b , angular frequency, mass density, thickness of the plate, and bending stiffness of the plate are related as:

$$k_b = (k_x^2 + k_y^2)^{1/4} = (\omega^2 \rho h / D)^{1/4} \quad (4)$$

Using Equation (4), the equations of motion can be obtained as follows:

$$(\nabla^4 - k_b^4) \bar{w}_p(x, y) = \frac{f_{pr}}{D}. \quad (5)$$

Using Equation (1b), the equations of motion can be obtained as Equation (6a). From the base excitation, the relation between vertical displacement of the plate and resonator can be expressed as Equation (6b):

$$(-\omega^2 m_r + k_r) \bar{w}_r = k_r \bar{w}_p, \quad (6a)$$

$$\bar{w}_r = \bar{w}_p \frac{k_r}{m_r(\omega_0^2 - \omega^2)}. \quad (6b)$$

where ω_0 is the natural resonance frequency of the mass–spring system. From the equilibrium of force between the resonator and plate, f_{pr} can be obtained as follows:

$$f_{pr} = k_r(\bar{w}_r - \bar{w}_p) = \omega^2 m_r \bar{w}_r. \quad (7)$$

By substituting Equation (7) in Equation (5), f_{pr} can be eliminated to obtain Equation (8a). Substituting Equation (6b) in Equation (8a) and rearranging the terms, an equation containing only the vertical displacement of the plate w_p can be obtained as follows:

$$(\nabla^4 - k_b^4) \bar{w}_p = \frac{1}{D} \omega^2 m_r \bar{w}_r, \quad (8a)$$

$$(\nabla^4 - k_b^4) \bar{w}_p = \frac{1}{D} \frac{\omega^2 m_r k_r}{m_r(\omega_0^2 - \omega^2)} \bar{w}_p, \quad (8b)$$

$$\left(\nabla^4 - \left(k_b^4 + \frac{1}{D} \frac{\omega^2 m_r k_r}{m_r(\omega_0^2 - \omega^2)} \right) \right) \bar{w}_p = 0. \quad (8c)$$

This equation is the modified Helmholtz equation for the plate on which the mass–spring resonators are uniformly distributed. From Equation (8c), the modified wavenumber can be obtained as follows:

$$k_{\text{mod}} = \left(k_b^4 + \frac{1}{D} \frac{\omega^2 m_r k_r}{(\omega_0^2 - \omega^2)} \right)^{1/4}. \quad (9)$$

Bandgap is defined as a frequency band where free waves do not propagate. To prevent wave propagation, the wavenumber has to be purely imaginary, which is the condition for an evanescent wave. Therefore, the modified wavenumber must satisfy the following condition:

$$k_b^4 + \frac{1}{D} \frac{\omega^2 m_r k_r}{(\omega_0^2 - \omega^2)} < 0 \quad (10a)$$

$$\omega^2 m_p + \frac{\omega^2 m_r k_r}{m_r(\omega_0^2 - \omega^2)} < 0 \quad (10b)$$

Eliminating m_r in the numerator and denominator of the second term and rearranging the remaining terms, Equation (10b) can be expressed as follows:

$$\omega^2 m_p + \frac{\omega^2 k_r}{\omega_0^2 - \omega^2} < 0 \quad (11a)$$

$$\omega^2 \left(m_p + \frac{k_r}{\omega_0^2 - \omega^2} \right) < 0 \quad (11b)$$

$$m_p + \frac{k_r}{\omega_0^2 - \omega^2} < 0 \quad (11c)$$

m_p is the mass of the plate, which is always positive. Therefore, the first condition for the equation to be negative is that $\omega > \omega_0$. This is the lower frequency limit; the upper frequency limit can be obtained by solving the inequality. Here, the total frequency bound is defined as

$$\omega_0 < \omega < \sqrt{\omega_0^2 + \frac{k_r}{m_p}} \quad (12)$$

The bandgap can be obtained from the difference between the upper and lower frequency limits. The upper frequency limit is related to the natural frequency; hence, the bandgap can be expressed in terms of natural frequency as

$$\begin{aligned} \Delta\omega_{BG} &= \omega_0(\sqrt{1 + m_r/m_p} - 1) \\ &= \omega_0(\sqrt{1 + M_r} - 1) \end{aligned} \quad (13)$$

$$\frac{\Delta\omega_{BG}}{\omega_0} = (\sqrt{1 + M_r} - 1). \quad (14)$$

where M_r is the mass ratio defining m_r/m_p . It can thus be observed that the resonant frequency as well as the mass ratio are important factors for determining the bandgap.

2.2. Serpentine Resonator

Figure 2 shows the serpentine resonator that consists of a combination of a rigid mass and serpentine beams, which correspond to the mass and spring of the system, respectively. The serpentine resonator can be divided into three parts. Parts 1 and 3 are in contact with the mass and plate, respectively. Part 2 connects parts 1 and 3 and it consists of N repeated segments; additionally, the serpentine resonator in Figure 2 is repeated twice. The symbols representing the length of each beam are shown in Figure 2 and Table 1. To simplify the calculation, we have assumed that $l_{ini} = l_{fin} = l_p$.

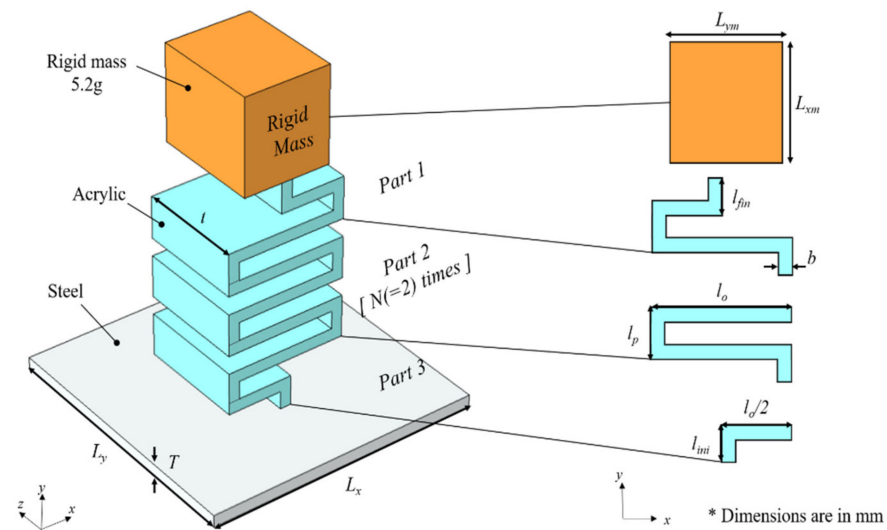


Figure 2. Concept of serpentine resonator.

Table 1. Symbols representing the length of the serpentine resonator.

Symbol	Definition
L_x	Length of the plate in x direction
L_z	Length of the plate in z direction
T	Thickness of the plate
L_{xm}	Length of the rigid mass in x direction
L_{ym}	Length of the rigid mass in y direction
t	Thickness of the serpentine beams
l_{ini}	Length of the initial beam
l_{fin}	Length of the final beam
l_o	Length of the beam orthogonal to the y-axis (vertical)
l_p	Length of the beam parallel to the y-axis (horizontal)
b	Width of the serpentine beams

Figure 3 shows the schematic of each part and their segment beams. The serpentine beams of each part are composed of horizontal and vertical beams. Part 1 consists of three horizontal beams and one and a half vertical beams; part 2 consists of two horizontal beams and two vertical beams, and part 3 consists of one horizontal beam, and half of a vertical beam. The section enclosed in a box with dotted lines in Figure 3 is the free-body diagram with forces and moments of the horizontal and vertical beams. The spring constant of the serpentine beam is derived using the principle of virtual work. The red arrow represents the virtual force exerted on the beam.

The formula for total energy in the bending beam is derived by integrating the strain energy density for each beam as follows:

$$U = \sum_{i=1}^m \left[\int_0^{l_p} \left(\frac{M^2}{2EI_{zp}} dx \right) \right]_i + \sum_{j=1}^n \left[\int_0^{l_o} \left(\frac{M^2}{2EI_{zo}} dy \right) \right]_j, \quad (15)$$

where M is the moment of the beam, E is the Young's modulus, and I_{zp} and I_{zo} are the moments of inertia of the horizontal and vertical beams, respectively. The first and second terms represent the energies of the horizontal and vertical beams, respectively. The moments of inertia of the horizontal and vertical beams are given as:

$$I_{zp} = \frac{1}{12} tb^3, \quad (16a)$$

$$I_{zo} = \frac{1}{12} tl_p^3, \quad (16b)$$

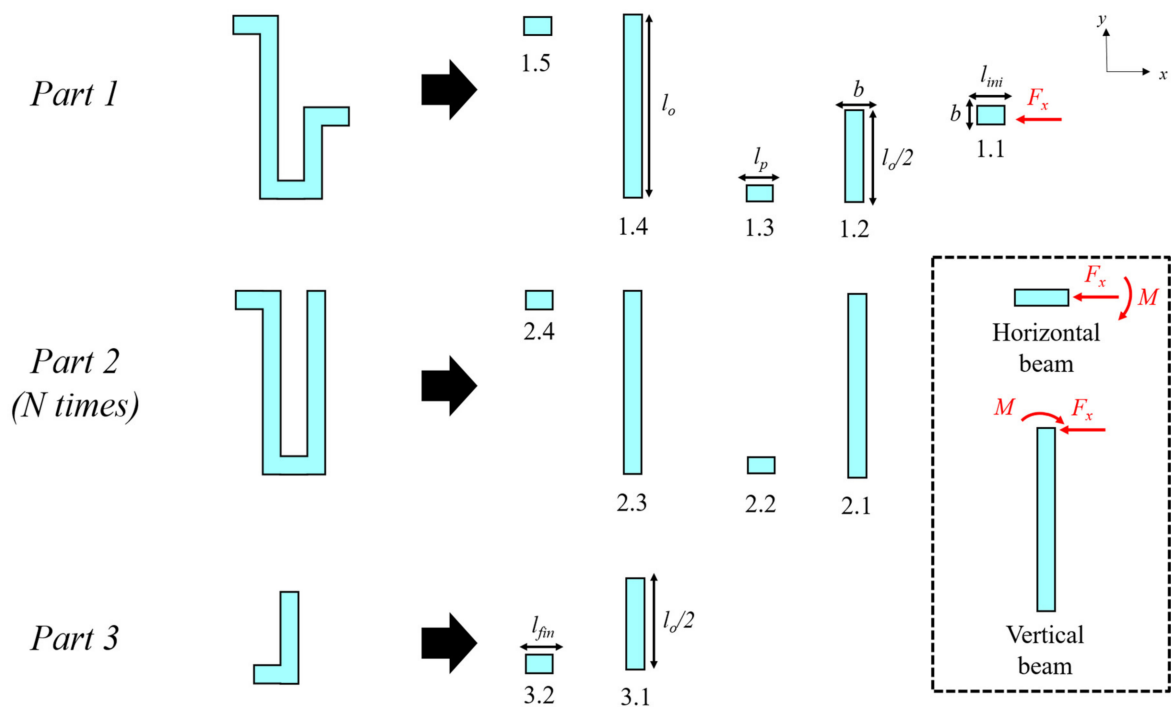


Figure 3. Schematic diagram of each part along with their segment beams.

Using the principle of virtual work, the displacement of the serpentine beams in the x-direction can be derived as:

$$\delta_x = \frac{\partial U}{\partial F_x} = \sum_{i=1}^m \left[\int_0^{l_p} \left(\frac{M}{EI_{zp}} \frac{\partial M}{\partial F_x} dx \right) \right]_i + \sum_{j=1}^n \left[\int_0^{l_o} \left(\frac{M}{EI_{zo}} \frac{\partial M}{\partial F_x} dy \right) \right]_j \quad (17)$$

Using Hooke's law to derive the spring constant, the displacement of the total serpentine beams can be expressed as:

$$k_x = \frac{F_x}{\delta_x}, \quad (18)$$

$$\begin{aligned} \delta_{x,tot} &= \delta_{1,1} + \delta_{1,2} + N(\delta_{2,1} + \delta_{2,2} + \delta_{2,3} + \delta_{2,4}) + (\delta_{3,1} + \delta_{3,2} + \delta_{3,3} + \delta_{3,4} + \delta_{3,5}), \\ &= \frac{(N+1)F_x l_o^3}{6EI_{zo}} + \frac{(N+1)F_x l_o^2 l_p}{2EI_{zp}}, \end{aligned} \quad (19)$$

where N is the number of times each part is repeated and F_x is the virtual force. Substituting the total displacement in the equation for Hooke's law, the spring constant of the serpentine beam can be obtained as:

$$k_x = \left[\frac{(N+1)l_o^3}{6EI_{zo}} + \frac{(N+1)l_o^2 l_p}{2EI_{zp}} \right]^{-1}, \quad (20)$$

Then, the resonant frequency of the serpentine resonator can be expressed as:

$$\omega_0 = \sqrt{\frac{1}{Sm_r} \left[\frac{(N+1)l_o^3}{6EI_{zo}} + \frac{(N+1)l_o^2 l_p}{2EI_{zp}} \right]^{-1}}, \quad (21)$$

Likewise, the bandgap of the serpentine resonator is derived as:

$$\Delta\omega_{BG} = \sqrt{\frac{1}{Sm_r} \left[\frac{(N+1)l_o^3}{6EI_{zo}} + \frac{(N+1)l_o^2 l_p}{2EI_{zp}} \right]^{-1}} \left(\sqrt{1 + M_r} - 1 \right) \quad (22)$$

3. Numerical Validation

3.1. Resonant Frequency

To validate the equations for resonant frequency and bandgap of the serpentine resonator derived in Section 2, the theoretical values were compared with the results of a finite element method (FEM) analysis. The FEM analysis was conducted through the 3D Multiphysics software COMSOL with eigenfrequency analysis. The analysis model is a serpentine resonator made of acrylic fixed to a steel plate, which is the host structure. The material properties of the acrylic were $E = 3.2$ GPa, Poisson's ratio of 0.4, mass density of 1165 kg/m^3 , and concentrated mass = 5.2 g with acrylic. Table 2 shows the list of dimensions used in the analysis model.

Table 2. Dimensions of the analysis model.

l_o	l_p	b	t	L_{xm}	L_{ym}	L_{xh}	L_{yh}	T
8.75 mm	2 mm	1 mm	10 mm	8 mm	8 mm	25 mm	25 mm	1 mm

Figure 4 shows the resonance frequencies and their mode shapes. Five resonance frequencies below 500 Hz are indicated in the figure. At the first and second resonance frequencies, the first bending mode appears. The two mode shapes differ only in the direction of vibration. At the fourth and fifth resonance frequencies, the second bending mode and torsional mode appear, respectively. At the third resonance frequency of 158 Hz, the longitudinal mode, which is the mode of interest in this study, appears. Comparing this frequency with the theoretical result of 151 Hz, it is observed that the theoretical and simulation values are similar and the cause of error is the simplification of the resonator model to reduce the simulation cost.

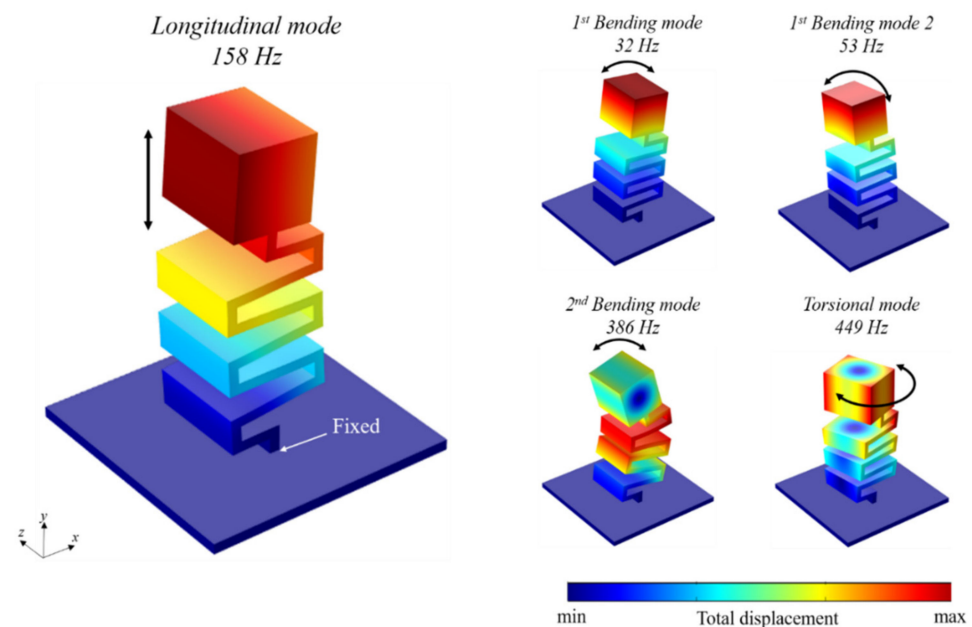


Figure 4. Mode shapes according to each resonance frequency.

Figure 5 shows an error map for the relative errors between simulation and theory with respect to l_p/b and l_o/b for different values of N . The other design parameters, namely, thickness and b , were set to 10 and 1 mm, respectively. N , l_p , and l_o were then modified to compare the third resonance frequency, which is the desired frequency.

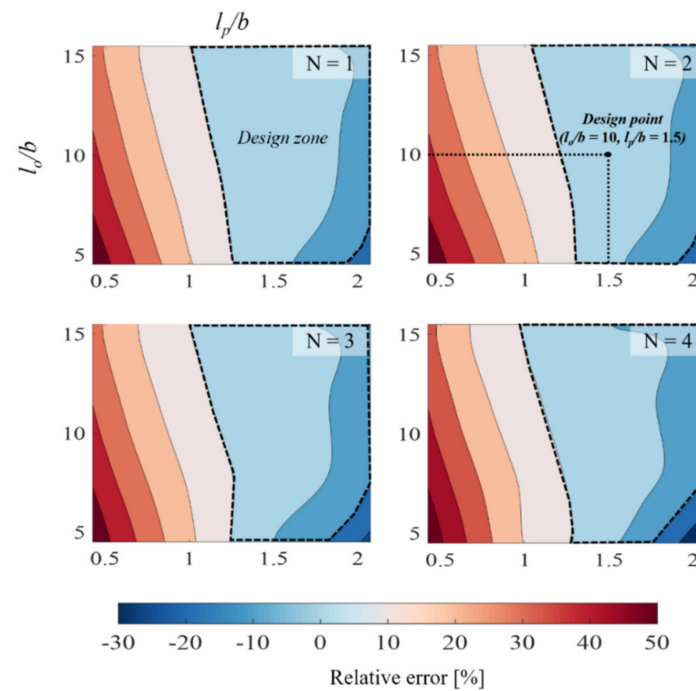


Figure 5. Relative error map for the resonance frequency of the serpentine resonator.

Figure 5 indicates that as l_p/b and l_o/b increase, the analysis result becomes stiffer than the theoretical result, and thus the error decreases. In the simulation, the total stiffness increases due to the geometric stiffness of the corner, which is not considered in the theoretical implementation. Additionally, the larger the joint, the less effective is the hypothesis of an ideal beam in theory. Hence, the simulation result becomes stiffer when the joints of the corners are larger. Similarly, when l_p/b is large, the simulation result becomes stiffer as N increases. Therefore, the parts indicated by the black dotted line are set as the design zone because the error of resonance frequency is small, and designing with parameter bounds in the design zone is considered reasonable.

3.2. Bandgap

Based on the design described in Section 3.1, the design parameters are set as $N = 2$, $l_p/b = 1.5$, and $l_o/b = 10$. This section describes the dispersion curve analysis that was conducted for the unit structure of the parameter in the design point of Figure 5 to compare the bandgap between the theoretical implementation and simulation. The dispersion curve is calculated by combining finite element (FE)-based unit cell modeling and Floquet–Bloch boundary conditions using COMSOL. For the analysis setting, a 25 mm steel plate was used as the host structure and a serpentine resonator was attached to the host structure, and this structure was repeated infinitely.

The dispersion curve analyzed with the above setting is shown in Figure 6. The shaded part highlighted in black is the bandgap generated based on FEM (COMSOL Multiphysics) analysis and the section enclosed in the box in red is the bandgap generated based on the theoretical implementation. The bandgap of the FEM ranges from 158 to 228 Hz and that for theoretical implementation ranges from 151 to 217 Hz. Figure 6b shows the mode shapes of the serpentine resonator unit structure. A and B are the Bloch mode shapes at the lower and upper bounds of the bandgap, respectively. A is the in-phase mode and B is the out-of-phase mode; C is the bending mode in x-axis and D is the bending mode in y-axis.

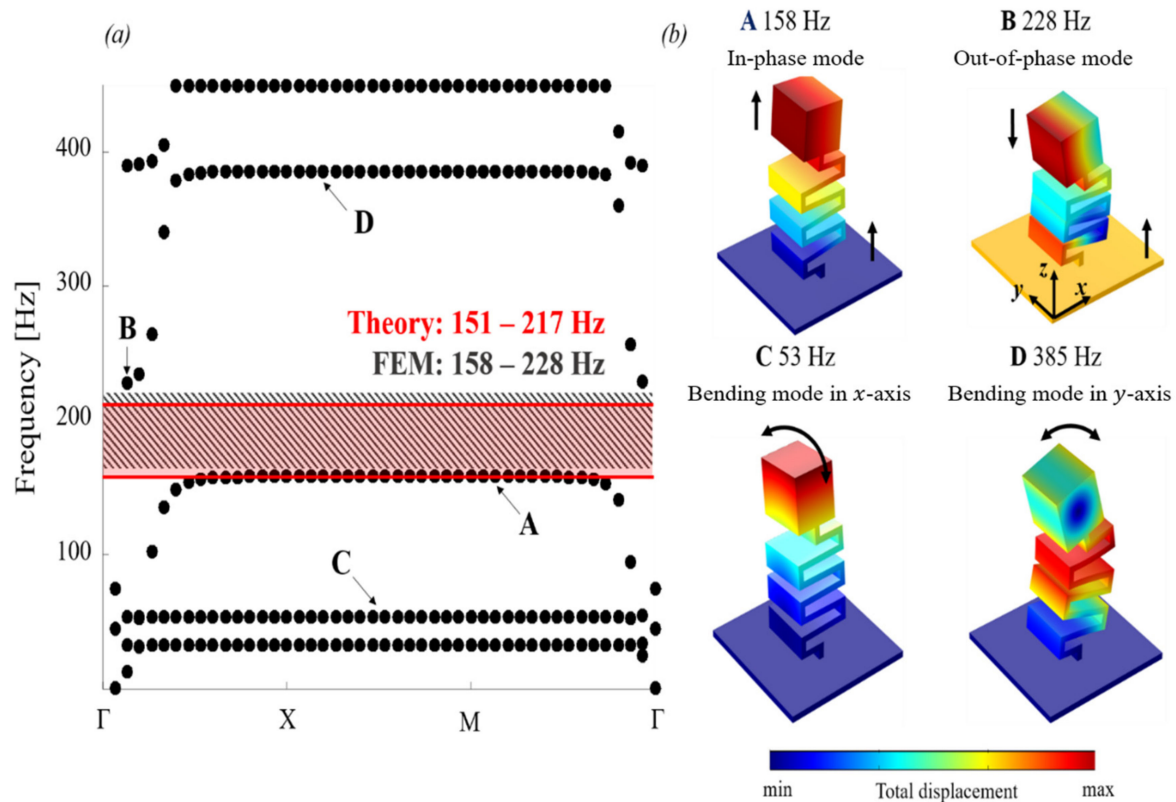


Figure 6. (a) Dispersion curve and (b) mode shapes of the analysis model.

The bandgaps for all the mode shapes are different from each other. The error of the bandgap result may be based on the following two reasons. The first is the simplification of the resonator model and the second is the simplification of the bandgap estimation theory. In the former, the analysis model is simplified to reduce the cost of the analysis, which induces the error. However, the error is negligible. In the latter, the conventional bandgap estimation theory begins with the unit structure modeling in which a mass–spring resonator is combined on a thin plate. This unit structure is deduced from the calculation of mass and spring matrices through the FEM analysis, and the dispersion relation is inferred based on the Floquet–Bloch theorem. Additionally, the dispersion curve is decided in the irreducible Brillouin-zone (IBZ) to estimate the bandgap.

However, the bandgap estimation theory proposed in this study is simply a theory based on the condition that the wave does not propagate through the wave equation. Therefore, the theory is prone to inevitable error. This can be attributed to the process of estimating the spring constant. It is assumed that the joint between the beams is ideal, but the larger the joint of the beam or the larger the thickness, the more invalid is this assumption. Since the bandgap estimation theory is related to the spring constant of the serpentine resonator, this error cannot be ignored.

Figure 7 shows the relative error of the resonance frequency and bandgap for N fixed at two and constant l_p when l_o/b is modified. The figure indicates that as the values of the parameters l_o and l_p increase, the relative bandgap error decreases, which is similar to the phenomenon when N changes. Therefore, for the experimental validation, we have considered $l_p = 1.5$ and $l_o/b = 10$, which have the lowest relative error.

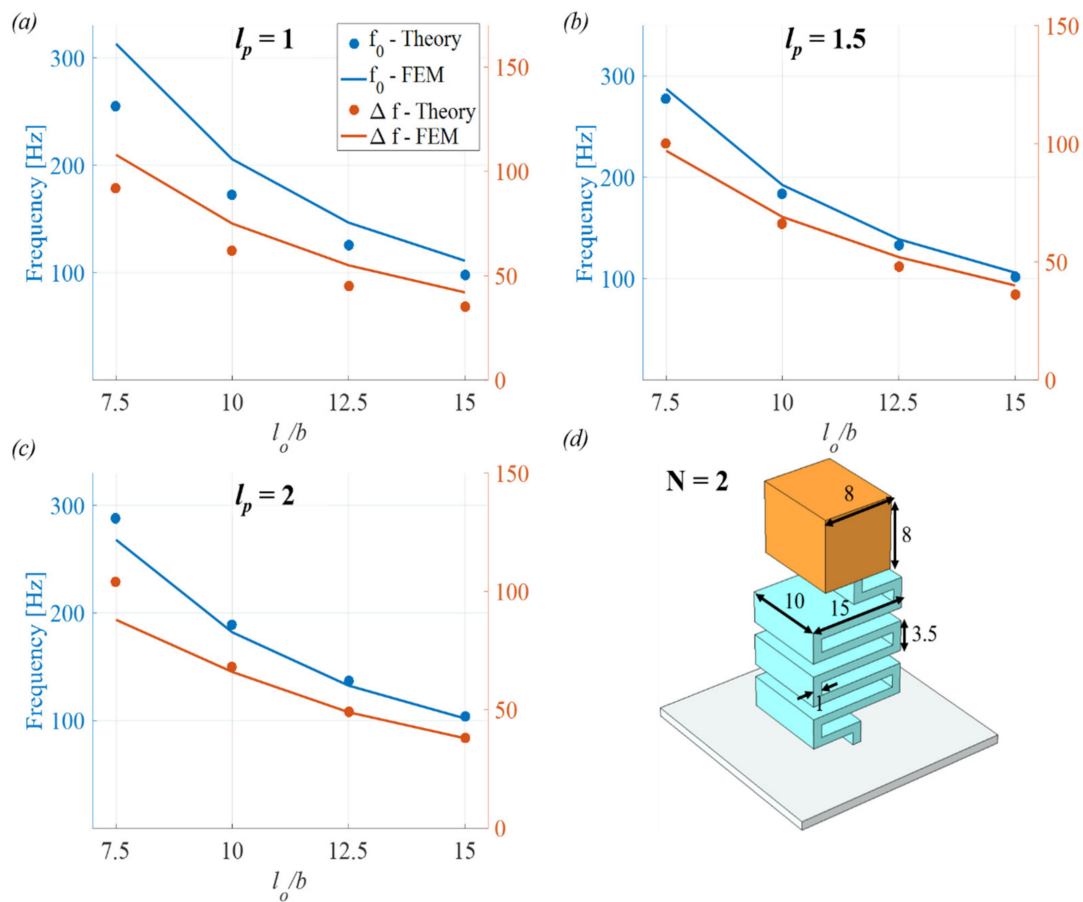


Figure 7. (a) Relative error of resonance frequency and bandgap when $N = 2$, $l_p = 1$, (b) $l_p = 1.5$, (c) $l_p = 2$, according to the change in l_o/b , and (d) unit structure.

4. Experimental Validation

4.1. Fabrication

The unit structure is designed as a serpentine resonator to experimentally verify the bandgap generated from the numerical results as shown in Figure 8. The serpentine resonator is made of acrylic material with elastic modulus $E = 3.2$ GPa, mass density $\rho = 1165$ kg/m³, and Poisson's ratio $\nu = 0.4$. The tip mass of the serpentine resonator is made of a nut & bolt pair, which weights 5.9 g, and it is assumed to be rigid in the desired frequency range. Table 3 shows the dimensions of the serpentine resonator used to generate the bandgap from 201–290 Hz within a cuttable width of 8 mm acrylic. Fabricated sample was manufactured by laser cutting and dimensions were changed due to manufacturing conditions. Dimensions were taken within the same design zone in Figure 5.

Figure 9a shows the dispersion curve of the fabricated sample and unit structure analyzed by a three-dimensional (3D) FE simulation using COMSOL Multiphysics. The shaded part highlighted in black is the bandgap generated based on FEM (COMSOL Multiphysics) and the section enclosed in the box in red is the bandgap generated based on the theoretical implementation. The bandgap generated through the FEM simulation ranges from 201 to 290 Hz and that generated by the theoretical implementation is in the range of 204–294 Hz. Figure 9b shows the mode shapes of the serpentine resonator unit structure. A and B are the Bloch mode shapes at the lower and upper bounds of the bandgap, respectively; A is in-phase mode, and B is out-of-phase mode. C is the bending mode in x-axis and D is the bending mode in y-axis.

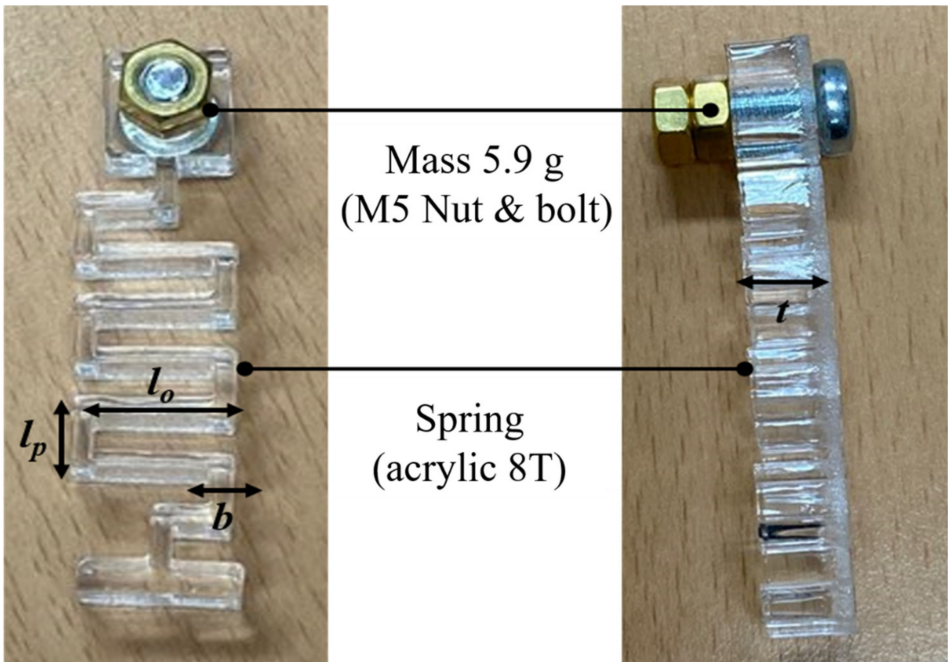


Figure 8. Fabricated serpentine resonator.

Table 3. Dimensions of the fabricated serpentine resonator.

l_o	l_p	b	t	L_{xm}	L_{ym}	L_{xh}	L_{yh}	T
15 mm	3 mm	2 mm	8 mm	12 mm	12 mm	25 mm	25 mm	1 mm

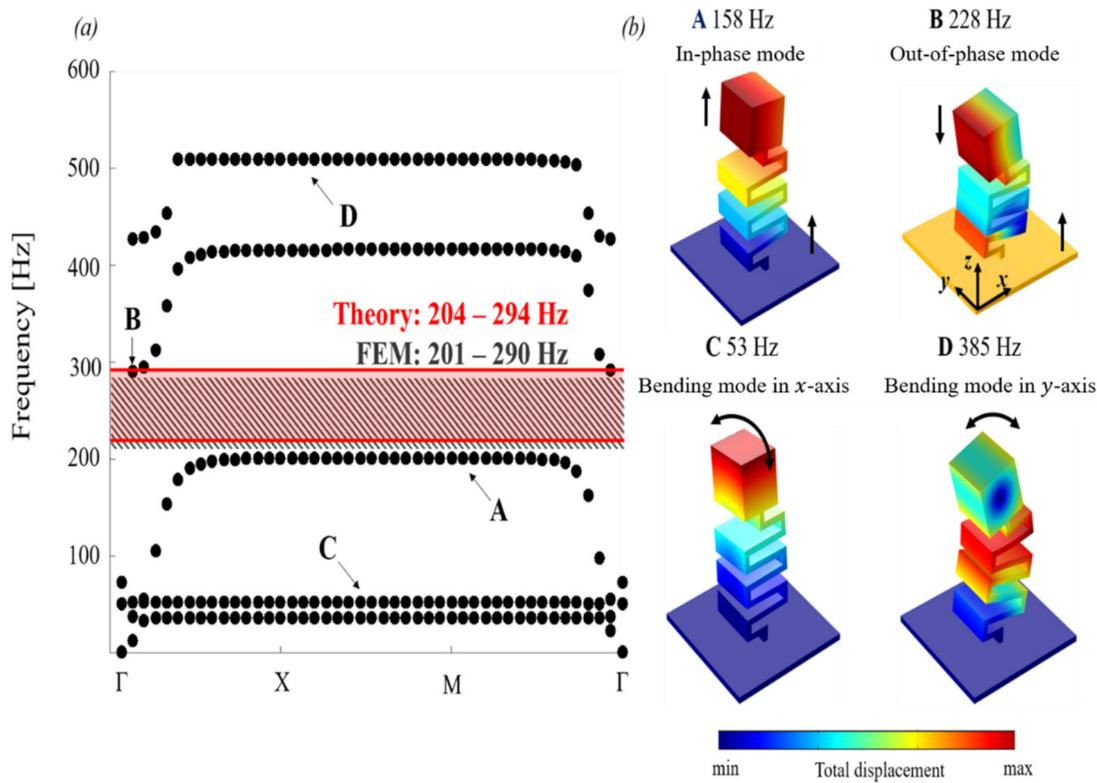


Figure 9. (a) Dispersion curve and (b) mode shapes of the fabricated sample.

The serpentine resonators are all cut with the same machine and acrylic plate to reduce process errors between samples. To evaluate the deviation between the FE model and fabricated samples, the resonance frequencies of five samples were measured. The fabricated samples were vertically attached with a silicon glue on the shaker to realize the fixed boundary condition, and the resonance frequencies were measured using laser scanning vibrometer (LSV) and compared with the FE model. Table 4 shows the resonance frequencies of the five samples. As shown in the table, the average frequency of the measurement results is 189 Hz, and the average is 190 Hz with the 3D FE simulation.

Table 4. Measured values of resonance frequency.

Sample	1	2	3	4	5	Average
Resonance [Hz]	189	188	193	190	186	189

4.2. Vibration Transmission

Figure 10 shows the vibration transmission experimental setup to analyze the vibration response of the fabricated serpentine resonators. A steel beam with dimensions 300×50 mm is used as the host structure. The serpentine resonators are arranged in a 2×10 array in intervals of 25 mm on a 1 mm-thick steel beam with silicone glue. The surface vibrational velocity of the serpentine resonators is measured using the impact hammer and accelerometer. To minimize the effect of mass, hammer excitation is performed instead of shaker excitation. The accelerometer is attached to a point 20 mm away from the end of the beam and the hammer point also vibrates at the same point. The steel beam is supported by wires so that all the edges are in the free–free boundary condition.

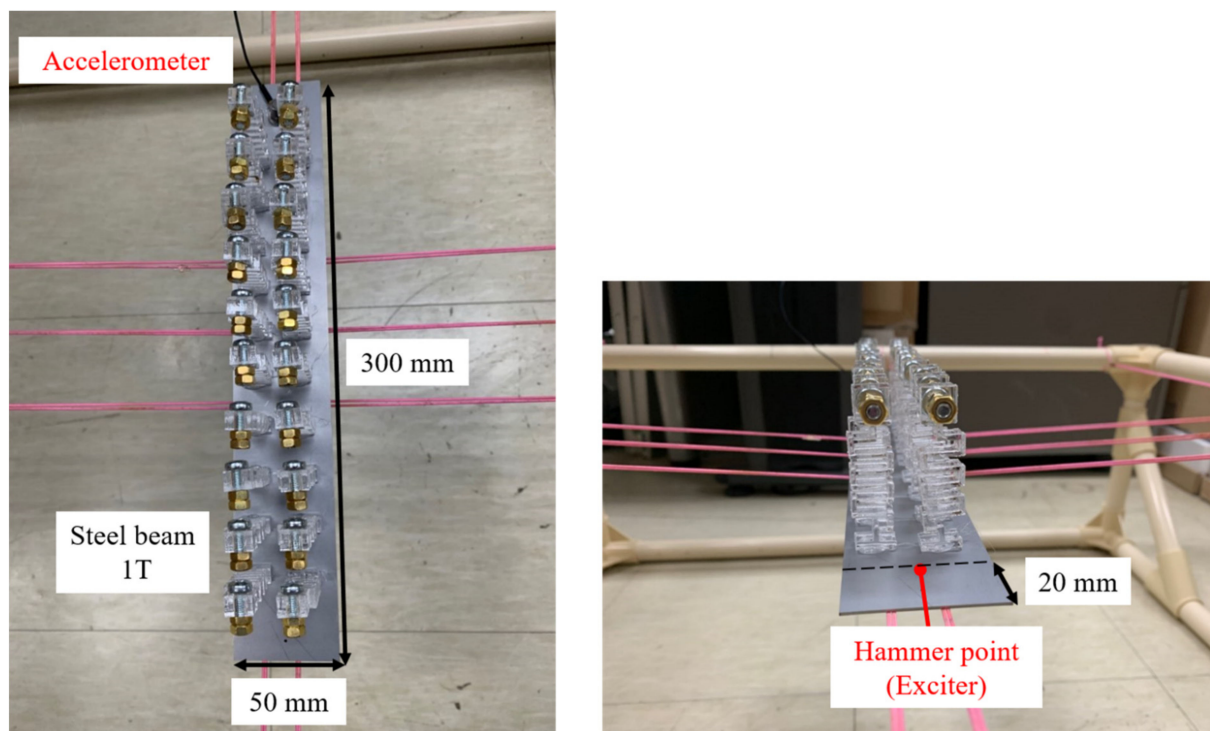


Figure 10. Experimental setup of vibration transmission.

Figure 11 displays the measurement result of the bare beam and serpentine resonator beam. The red and green lines represent the vibration responses of the two beams, respectively. The measurement result shows that the vibration response of the serpentine resonator is significantly reduced for the bandgap in the range of 200–290 Hz. In frequency

bands other than the bandgap, the peaks are shifted and reduced due to damping and mass effects. However, in the bandgap, the result shows that the dip is divided into several peaks because of the local modes of the serpentine resonator. The figure also shows that the measurement results for the bandgap region obtained by theoretical implementation and simulation are similar.

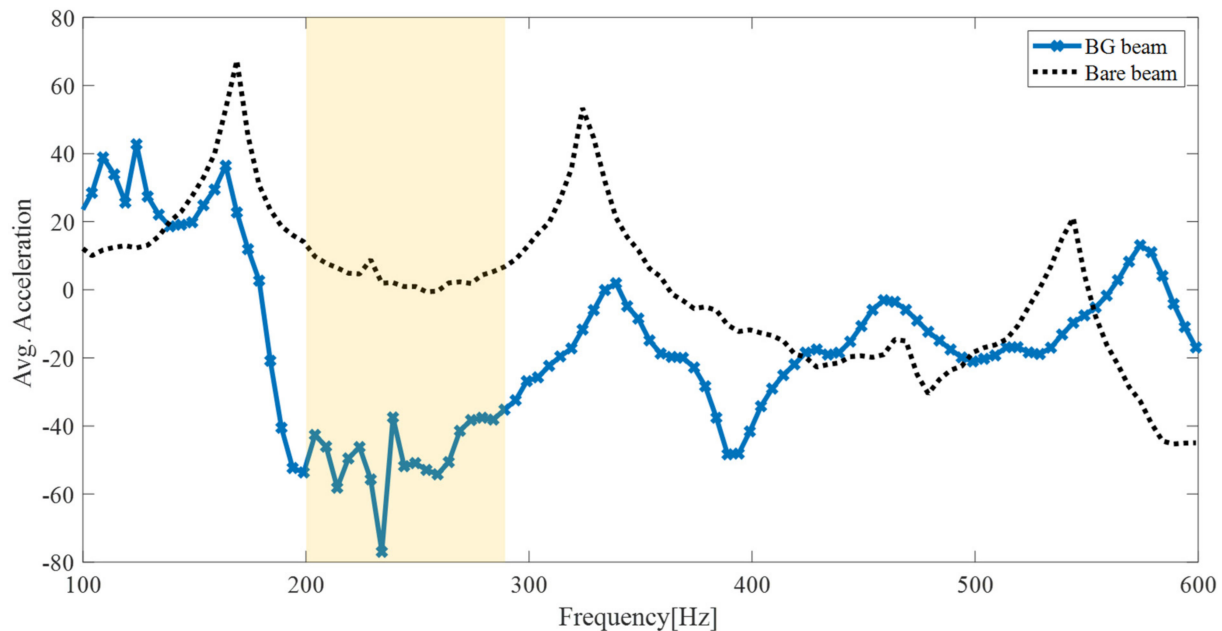


Figure 11. Vibration measurement result.

5. Conclusions

In this study, we presented the derivation of an equation for a bandgap based on a numerical and experimental approach. A simplified model consisting of a resonator (mass–spring system) and host structure was used to derive the equation. Since the resonator was used as a serpentine resonator, the design freedom of the bandgap increased; hence, various design parameters of the simplified model were used to control the bandgap. The simplified model was simulated to verify the theoretical equation using commercial software. The resonant frequency and bandgap of the serpentine resonator were calculated and compared with the theoretical result to analyze the cause of relative error. In addition, the relative error map for each design variable was also presented to confirm the critical design variables. Experimental validation was conducted to verify the theoretical equation. The experiment was conducted using an impact hammer test, and the bandgap effect and vibration reduction on the thin beam were confirmed. The serpentine resonator reduces vibration by 5.5 dB in the bandgap frequency region and this is in agreement with the theoretical implementation and simulation. Therefore, the bandgap equation solved numerically through software in this study is mathematically derived for the first time. The derived bandgap equation can be used to control the bandgap by adjusting the design parameters, and the time used for simulation can be significantly shortened. Furthermore, if this study is limited to tortuous resonators, it is expected that it will be possible to derive bandgaps of various unit structures if developed.

Author Contributions: J.Y.: Conceptualization, Methodology, Software, Formal analysis, Visualization, Writing—original draft; J.J.: Conceptualization, Investigation; S.W.: Supervision, Funding acquisition. All authors have read and agreed to the published version of the manuscript.

Funding: This study was supported by the National Research Foundation of Korea (NRF) grant funded by the Korean government (MSIT) (NO.2021R1A2C2013259).

Institutional Review Board Statement: Not applicable.

Informed Consent Statement: Not applicable.

Data Availability Statement: All data in this paper are available, there are no additional data.

Conflicts of Interest: The authors declare that they have no known competing financial interests or personal relationships that could have appeared to influence the work reported in this paper.

References

- Shin, D.; Urzhumov, Y.; Jung, Y.; Kang, G.; Baek, S.; Choi, M.; Park, H.; Kim, K.; Smith, D.R. Broadband electromagnetic cloaking with smart metamaterials. *Nat. Commun.* **2012**, *3*, 1213. [\[CrossRef\]](#) [\[PubMed\]](#)
- Pendry, J.B. Controlling Electromagnetic Fields. *Science* **2006**, *312*, 1780–1782. [\[CrossRef\]](#)
- Schurig, D.; Mock, J.J.; Justice, B.J.; Cummer, S.A.; Pendry, J.B.; Starr, A.F.; Smith, D.R. Metamaterial Electromagnetic Cloak at Microwave Frequencies. *Science* **2006**, *314*, 977–980. [\[CrossRef\]](#) [\[PubMed\]](#)
- Fu, P.; Liu, F.; Ren, G.J.; Su, F.; Li, D.; Yao, J.Q. A broadband metamaterial absorber based on multi-layer graphene in the terahertz region. *Opt. Commun.* **2018**, *417*, 62–66. [\[CrossRef\]](#)
- Samson, Z.L.; MacDonald, K.F.; De Angelis, F.; Gholipour, B.; Knight, K.; Huang, C.C.; Di Fabrizio, E.; Hewak, D.W.; Zheludev, N. Metamaterial electro-optic switch of nanoscale thickness. *Appl. Phys. Lett.* **2010**, *96*, 143105. [\[CrossRef\]](#)
- Toal, B.; McMillen, M.; Murphy, A.; Hendren, W.; Atkinson, R.; Pollard, R. Tuneable magneto-optical metamaterials based on photonic resonances in nickel nanorod arrays. *Mater. Res. Express* **2014**, *1*, 015801. [\[CrossRef\]](#)
- Pai, P.F.; Peng, H.; Jiang, S. Acoustic metamaterial beams based on multi-frequency vibration absorbers. *Int. J. Mech. Sci.* **2014**, *79*, 195–205. [\[CrossRef\]](#)
- Lee, S.H.; Park, C.M.; Seo, Y.M.; Wang, Z.G.; Kim, C.K. Acoustic metamaterial with negative density. *Phys. Lett. A* **2009**, *373*, 4464–4469. [\[CrossRef\]](#)
- Ma, G.; Sheng, P. Acoustic metamaterials: From local resonances to broad horizons. *Sci. Adv.* **2016**, *2*, e1501595. [\[CrossRef\]](#)
- Mei, J.; Ma, G.; Yang, M.; Yang, Z.; Wen, W.; Sheng, P. Dark acoustic metamaterials as super absorbers for low-frequency sound. *Nat. Commun.* **2012**, *3*, 756. [\[CrossRef\]](#)
- Sui, N.; Yan, X.; Huang, T.Y.; Xu, J.; Yuan, F.G.; Jing, Y. A lightweight yet sound-proof honeycomb acoustic metamaterial. *Appl. Phys. Lett.* **2015**, *106*, 171905. [\[CrossRef\]](#)
- Liu, Z.; Rumpler, R.; Feng, L. Locally resonant metamaterial curved double wall to improve sound insulation at the ring frequency and mass-spring-mass resonance. *Mech. Syst. Signal Process.* **2021**, *149*, 107179. [\[CrossRef\]](#)
- Wang, Y.-Z.; Ma, L. Sound insulation performance of membrane-type metamaterials combined with pyramidal truss core sandwich structure. *Compos. Struct.* **2021**, *260*, 113257. [\[CrossRef\]](#)
- Krushynska, A.O.; Kouznetsova, V.G.; Geers, M.G.D. Towards optimal design of locally resonant acoustic metamaterials. *J. Mech. Phys. Solids* **2014**, *71*, 179–196. [\[CrossRef\]](#)
- Naify, C.J.; Chang, C.-M.; McKnight, G.; Nutt, S. Transmission loss and dynamic response of membrane-type locally resonant acoustic metamaterials. *J. Appl. Phys.* **2010**, *108*, 114905. [\[CrossRef\]](#)
- Yu, J.; Nerse, C.; Chang, K.; Wang, S. A framework of flexible locally resonant metamaterials for attachment to curved structures. *Int. J. Mech. Sci.* **2021**, *204*, 106533. [\[CrossRef\]](#)
- Claeys, C.; Deckers, E.; Pluymers, B.; Desmet, W. A lightweight vibro-acoustic metamaterial demonstrator: Numerical and experimental investigation. *Mech. Syst. Signal Process.* **2016**, *70*, 853–880. [\[CrossRef\]](#)
- Claeys, C.; de Melo Filho, N.G.R.; Van Belle, L.; Deckers, E.; Desmet, W. Design and validation of metamaterials for multiple structural stop bands in waveguides. *Extrem. Mech. Lett.* **2017**, *12*, 7–22. [\[CrossRef\]](#)
- De Melo Filho, N.G.R.; Belle, V.L.; Claeys, C.; Deckers, E.; Desmet, W. Dynamic mass based sound transmission loss prediction of vibro-acoustic metamaterial double panels applied to the mass-air-mass resonance. *J. Sound Vib.* **2019**, *442*, 28–44. [\[CrossRef\]](#)
- Sangiuliano, L.; Claeys, C.; Deckers, E.; Desmet, W. Influence of boundary conditions on the stop band effect in finite locally resonant metamaterial beams. *J. Sound Vib.* **2020**, *473*, 115225. [\[CrossRef\]](#)
- Nateghi, A.; Belle, V.L.; Claeys, C.; Deckers, E.; Pluymers, B.; Desmet, W. Wave propagation in locally resonant cylindrically curved metamaterial panels. *Int. J. Mech. Sci.* **2017**, *127*, 73–90. [\[CrossRef\]](#)
- Wang, Q. Bandgap properties in metamaterial sandwich plate with periodically embedded plate-type resonators. *Mech. Syst. Signal Process.* **2021**, *13*, 107375. [\[CrossRef\]](#)
- Jung, J.; Kim, H.G.; Goo, S.; Chang, K.J.; Wang, S. Realisation of a locally resonant metamaterial on the automobile panel structure to reduce noise radiation. *Mech. Syst. Signal Process.* **2019**, *122*, 206–231. [\[CrossRef\]](#)
- Chang, I.-L.; Liang, Z.-X.; Kao, H.-W.; Chang, S.-H.; Yang, C.-Y. The wave attenuation mechanism of the periodic local resonant metamaterial. *J. Sound Vib.* **2018**, *412*, 349–359. [\[CrossRef\]](#)
- Fang, X.; Wen, J.; Yin, J.; Yu, D. Wave propagation in nonlinear metamaterial multi-atomic chains based on homotopy method. *AIP Adv.* **2016**, *6*, 121706. [\[CrossRef\]](#)
- Sugino, C.; Leadenham, S.; Ruzzene, M.; Erturk, A. On the mechanism of bandgap formation in locally resonant finite elastic metamaterials. *J. Appl. Phys.* **2016**, *120*, 134501. [\[CrossRef\]](#)
- Barillaro, G.; Molfese, A.; Nannini, A.; Pieri, F. Analysis, simulation and relative performances of two kinds of serpentine springs. *J. Micromech. Microeng.* **2005**, *15*, 736–746. [\[CrossRef\]](#)

28. Chou, H.-M.; Lin, M.-J.; Chen, R. Investigation of mechanics properties of an awl-shaped serpentine microspring for in-plane displacement with low spring constant-to-layout area. *J. Micro/Nanolith. MEMS MOEMS* **2016**, *15*, 035003. [[CrossRef](#)]
29. Park, B.; Afsharipour, E.; Chrusch, D.; Shafai, C.; Andersen, D.; Burley, G. Large displacement bi-directional out-of-plane Lorentz actuator array for surface manipulation. *J. Micromech. Microeng.* **2017**, *27*, 085005. [[CrossRef](#)]
30. Lishchynska, M.; Cordero, N.; Slattery, O.; O'Mahony, C. Spring Constant Models for Analysis and Design of MEMS Plates on Straight or Meander Tethers. *Sens. Lett.* **2006**, *4*, 200–205. [[CrossRef](#)]